

## Laboratory experiments simulating solar wind driven magnetospheres

P. Brady,<sup>1,a)</sup> T. Ditmire,<sup>1</sup> W. Horton,<sup>2</sup> M. L. Mays,<sup>2</sup> and Y. Zakharov<sup>3</sup>

<sup>1</sup>*Fusion Research Center, The University of Texas at Austin, Austin, Texas 78712, USA*

<sup>2</sup>*Institute for Fusion Studies, The University of Texas at Austin, Austin, Texas 78712, USA*

<sup>3</sup>*Institute of Laser Physics, Russian Academy of Sciences, Novosibirsk 630090, Av. Lavrentyeva 13/3, Russia*

(Received 27 August 2008; accepted 28 January 2009; published online 21 April 2009)

Magnetosphere-solar wind interactions are simulated in a laboratory setting with a small permanent magnet driven by two types of supersonic plasma wind sources. The first higher speed, shorter duration plasma wind is from a laser blow-off plasma while the second longer duration, lower speed plasma wind is produced with a capacitor discharge driven coaxial electrode creating plasma jets. The stand off distance of the solar wind from the magnetosphere was measured to be  $1.7 \pm 0.3$  cm for the laser-produced plasma experiment and  $0.87 \pm 0.03$  cm for the coaxial electrode plasma experiment. The stand off distance of the plasma was calculated using data from HYADES [J. T. Larsen and S. M. Lane, *J. Quant. Spectrosc. Radiat. Transf.* **51**, 179 (1994)] as  $1.46 \pm 0.02$  cm for the laser-produced plasma, and estimated for the coaxial plasma jet as  $r_{mp} = 0.72 \pm 0.07$  cm. Plasma build up on the poles of the magnets, consistent with magnetosphere systems, was also observed.

© 2009 American Institute of Physics. [DOI: 10.1063/1.3085786]

### I. INTRODUCTION

Laboratory astrophysical experiments need magnetohydrodynamic (MHD) scaling to justify comparison physics.<sup>1,2</sup> Gravity is a key physical force in astrophysical problems which is not present in laboratory simulations. In laboratory simulations of the solar wind driven magnetospheres gravity plays no significant role. The scaling factor from the laboratory to the solar-magnetospheric system is relatively small compared to other astrophysical phenomena.<sup>3-5</sup> The geophysical-laboratory scaling factor is  $10^9$  compared to that for a supernova,  $10^{13}$ , and with that for the eagle nebula,  $10^{20}$ .<sup>5</sup> The parameters for the solar wind-magnetosphere compared to the values in the laboratory simulation are shown in Table I. In this research we investigate effects that can be considered ideal MHD where dissipative effects such as viscosity, thermal conductivity, and radiative cooling are unimportant in the system.<sup>3</sup> In this study we investigate large scale MHD phenomena such as the magnetopause. Owing to the small space scales of the laboratory magnetosphere of order a few centimeters, no attempt is made to determine the microscale phenomena in magnetospheres with the laboratory experiments. The magnetic Reynolds number and other factors will also not be similar between the two frames. In laboratory simulations of astrophysical phenomena it is common that only a few of the dimensionless parameters have the same values between the two physical systems. We then keep in mind the differences that may occur from a lack of similarity between other parameters.

In astrophysical simulations the geometry of the set up should be similar to astrophysical case. In this experiment the geometry is straight forward with a plasma source impinging on a magnetic dipole. One flaw that cannot be remedied in our situation is that the plasma source is much more proximate to the dipole than any astrophysical solar wind

source is to a planetary dipole. Other comparisons can be made such as mach number. A further discussion about scaling is given in Sec. V.

In Table I we list parameters of Earth's magnetosphere from literature<sup>4,6</sup> and the corresponding value for the experiment in the second column. The hydrodynamic code HYADES, which will be discussed in Sec. V, derived the values in the second column for base line analysis and prediction. Earth's magnetosphere is a high temperature low density plasma that flows with large velocities. The length scale,  $h$ , is the distance of the magnetopause to the dipole center. The time scale  $t$  is taken as the length scale divided by the velocity of the solar wind. The solar wind plasma consists mainly of protons, while in contrast the experimental density consists of aluminum ions. This must be taken into account when comparing densities. This discussion of the parameters is revisited, in the context of scaling, in the analysis Sec. V.

In Sec. II we discuss the global dynamics of the plasma wind driven magnetosphere system. In Sec. III we discuss the experimental configurations and the diagnostic systems. In Sec. IV basic results of the experiments are shown, and in Sec. V we compare the observations with simulations using the HYADES hydrodynamic code. Section VI gives the conclusions suggested future experiments.

### II. DYNAMICS OF THE SOLAR WIND-MAGNETOSPHERE SYSTEM

The dynamics of the magnetosphere is driven by the solar wind which, in the experiment, is the blow-off plasma shown in Fig. 1.<sup>6,7</sup> The following MHD equations are a one-dimensional model of the global system:

$$\frac{\partial \rho}{\partial t} = - \frac{\partial}{\partial x}(\rho u), \quad (1)$$

<sup>a)</sup>Electronic mail: pbrady@physics.utexas.edu.

TABLE I. The parameters of Earth's magnetosphere are listed in the first column (Refs. 4 and 6). Scaling relations for Earth's magnetosphere and the experimental setting as calculated by HYADES (see Sec. V) are listed in the second column. The scaling parameters are  $a \approx 10^9$  (length scale ratio parameter),  $b \approx 10^{-15}$  (mass density scale ratio parameter), and  $c \approx 10^{-13}$  (pressure scale ratio parameter).

|                          | Solar wind/<br>magnetopause | Laser-produced<br>plasma | Coaxial<br>electrode jet |
|--------------------------|-----------------------------|--------------------------|--------------------------|
| $h$ (cm)                 | $10^9$                      | 1                        | 1                        |
| $t$ (s)                  | $10^2$                      | $10^{-7}$                | $10^{-6}$                |
| $n$ ( $\text{cm}^{-3}$ ) | 10                          | $10^{14}$                | $10^{15}$                |
| $T$ (eV)                 | 10                          | 5                        | 7                        |
| $B$ (G)                  | $10^{-4}$                   | $10^3$                   | $10^3$                   |
| $u$ (cm/s)               | $4.5 \times 10^7$           | $10^7$                   | $10^6$                   |
| $E_u$                    | 5–10                        | 4–10                     | 2                        |

$$\frac{\partial(\rho u)}{\partial t} = -\frac{\partial}{\partial r} \left( \rho u^2 + P + \frac{B^2}{2\mu_0} \right) - \frac{B^2}{\mu_0 R_c}, \quad (2)$$

where the term  $B^2/\mu_0 R_c$  is the magnetic field tension. When formulating the one-dimensional dynamics of the magnetosphere one needs to include a term for the magnetic tension, in which  $R_c$  is the radius of curvature of the magnetic field on the equatorial plane of the magnetosphere and  $B$  is the magnetic field strength. The magnetic field  $B$  is composed of the sum of the dipole field  $B_{dp}$  and the field  $\Delta B$  produced by the plasma currents. Using  $r$  as the distance from the dipole in the equatorial plane we have  $B_{dp}(r) = B_{R_{dp}}(R_{dp}/r)^3$  where  $R_{dp}$  is the radius of the magnet and  $R_c = r/3$  is the radius of curvature of the magnetic field lines crossing the equatorial plane at the distance  $r$  from the dipole.

In Eq. (1),  $\rho$  is the mass density of the plasma and  $u$  is the flow velocity. In absence of plasma  $\rho=0$ , the pressure,  $P$ , vanishes, and the outward magnetic pressure gradient balances the inward force of tension  $F_T = -\partial/\partial r(B_{dp}^2/2\mu_0) = 3B_{dp}^2/\mu_0 r$ . With the plasma present  $\rho \neq 0$ , and a boundary layer called the magnetopause forms as we now calculate.

The standoff distance,  $r_{mp}$  of the magnetopause, or the distance between the magnetopause and the magnetic dipole center, can be estimated by enforcing pressure balance of the solar wind dynamic pressure with the dipole magnetic field pressure

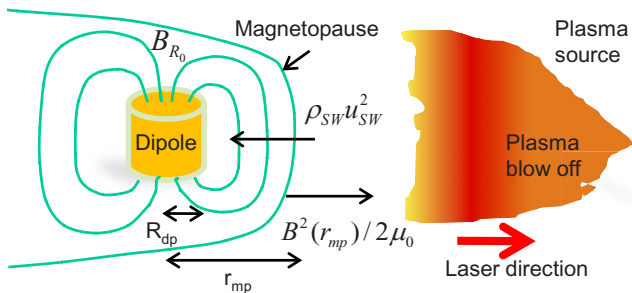


FIG. 1. (Color online) The laboratory experiment involved impinging a laser beam on an aluminum wire target creating a blow-off plasma which serves as a laboratory model for the solar plasma wind. The magnetopause is the boundary between the magnetosphere and the plasma wind where the magnetic pressure balances with the plasma wind pressure.

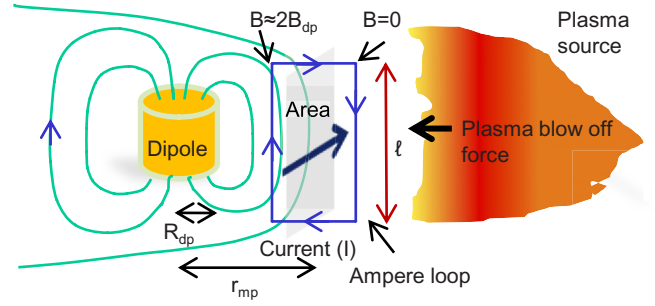


FIG. 2. (Color online) The plasma wind action on the magnetic field cause a current,  $I$ , to form on the magnetopause. The calculation of this current can be found by forming an Ampere loop around the magnetopause and observing that the magnetic field upstream of the magnetopause is zero.

$$\rho_{SW} u_{SW}^2 = B^2(r_{mp})/2\mu_0, \quad (3)$$

as illustrated in Fig. 1. We can eliminate the thermal pressure,  $P$ , in this analysis because the solar wind flow velocity is supersonic and thus the flow pressure,  $\rho_{SW} u_{SW}^2$ , will be much larger than the thermal pressure. The magnetic tension term can also be ignored because the introduction of a strong solar wind will flatten or compress the magnetopause on the equatorial plane and thus significantly reduce the magnetic tension. Using the mirror method formulation<sup>8</sup> to satisfy the boundary conditions at  $r_{mp}$ , the magnetic field at the magnetopause will be approximately twice the magnetic field as there would be without a solar wind interaction. Thus, in this approximation,  $B = B_{dp} + \Delta B \approx 2B_{dp}$  at the nose of the magnetopause. The dipole magnetic field pressure,  $P_{dp}(r)$  drops off as the sixth power of the distance

$$P_{dp}(r) = \frac{B_{dp}^2}{2\mu_0} = \frac{B_{R_{dp}}^2}{2\mu_0} \left( \frac{R_{dp}}{r_{mp}} \right)^6. \quad (4)$$

Then one calculates the standoff distance of the magnetopause as

$$r_{mp} = R_{dp} \left( \frac{2B_{R_{dp}}^2}{\mu_0 \rho_{SW} u_{SW}^2} \right)^{1/6}. \quad (5)$$

The dynamic pressure in the experiment is a pulse in time so that  $r_{mp}(t) = R_{dp} (2B_{R_{dp}}^2 / \mu_0 \rho_{SW} u_{SW}^2)^{1/6}$  is the time dependent position of the magnetopause. This corresponds to the compression and decompression measured in Earth's magnetopause during the transit of shocks and fronts from coronal mass ejections. Earth's magnetopause can be pushed in for short durations to where the geosynchronous satellites at  $R = 6.6R_E$  are beyond the magnetopause.

As the solar wind interacts with the dipole magnetic field it induces a force on the field. This causes a current to flow called the Chapman–Ferraro current (as shown in Fig. 2).<sup>9</sup> This current,  $I$ , alters the magnetic field in the magnetosphere to  $B_{ms} = B_{dp} + \Delta B$  and as such changes the magnetic field on Earth's surface. This current induced change  $\Delta B$  at the surface can be formulated by noting that the magnetic field has a sharp boundary at the magnetopause, quickly going to zero up stream from the magnetopause. The Chapman–Ferraro current can be estimated using the force-current equations,

by defining an effective flat area of the magnetopause cross section, and using the solar wind pressure on this area to obtain

$$F = \text{area} \times P_{\text{SW}} = I_{\text{CF}} \ell B_z. \quad (6)$$

The Chapman–Ferraro current can also be calculated from Ampere’s law as  $\ell \Delta B_z = \mu_0 I_{\text{CF}}$ , where  $\ell$  is the length of the side of an idealized Ampere rectangle encompassing the magnetopause as in Fig. 2. The  $\Delta B_z$  is the jump in the magnetic field on the magnetopause, which will be approximately  $2B_{\text{dp}}(r_{\text{mp}})$  since there is no magnetic field upstream of the magnetopause, and  $I_{\text{CF}}$  is the Chapman–Ferraro current. More details on the current loops driven by the plasma wind interaction with the dipole field are given in Ref. 10.

### III. EXPERIMENTAL CONFIGURATIONS AND DIAGNOSTICS

We designed a laboratory experiment to test the feasibility of studying scaled planetary magnetosphere physics in the laboratory. Laser-produced plasma and laser-triggered coaxial electrode plasma jets simulated a “solar wind” in the experiment. Permanent magnetic dipoles and nonmagnetic objects of the same size and shape were inserted in the path of this plasma wind as in Fig. 1. The goal of the experimental investigation was to investigate the creation of a shock front colliding with the magnetosphere while investigating the boundary of the magnetopause, and the plasma wind-magnetosphere interaction.

We use the two different plasma sources: (1) the laser-produced plasma and (2) coaxial electrode plasma jets. Both sources were available in the same experimental setup associated with the YOGA laser at the University of Texas. Both plasma sources had similar energies and velocities with some important differences. The laser-produced plasma had velocities about two to three times higher than the coaxial electrode jet, but the duration ( $\Delta t_1 \approx 400$  ns) of the laser-produced plasma flow is about 20% of the jet flow time ( $\Delta t_{\text{jet}} \approx 2000$  ns). In reference to the laser-produced plasma we have favorable comparisons with a simulation from HYADES. However the laser-produced plasma case provides a short time scale event in which the plasma parameters do not remain constant. In the coaxial plasma jet case the plasma parameters are essentially steady for  $\Delta t_{\text{jet}} \approx 2 \mu\text{s}$ , but have less reliable ways of determining their plasma parameters. Both methods gave measurements of a magnetopause that are reported in Sec. V.

The YOGA laser was capable of giving a 1064 nm, 8 ns pulse laser with energies up to  $3.7 \pm 0.2$  J. The interaction took place in a 12 L vacuum chamber that had a vacuum of 1.0 mTorr. A Princeton Instruments intensified charged coupled device (ICCD) camera with a 4.0 ns exposure time was the main diagnostic. The detection wavelength range was 350–575 nm due to the filters used on the camera. Interferometry was also used to characterize the densities of both plasma sources but the sensitivity was limited to plasmas very early in the expansion where the magnetosphere physics

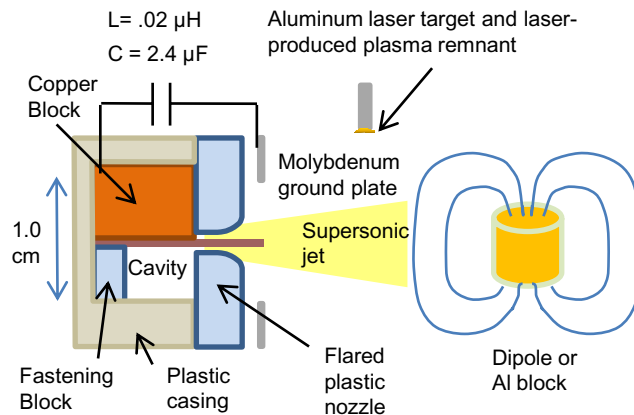


FIG. 3. (Color online) A plasma jet from a capacitor driven coaxial electrode device was used to create a plasma wind for a magnetosphere experiment. The plasma jet is formed by ablation of a molybdenum electrode from a capacitor bank discharge, combined with electrodynamic  $\mathbf{J} \times \mathbf{B}$  plasma acceleration forces. The discharge was triggered with a laser-produced plasma.

would not be important. Because of the small scale of the laboratory plasma ( $r_{\text{mp}} < 2$  cm) mm size direct probes were not used in the experiment.

A plasma wind was made using a coaxial device constructed to study plasma jets.<sup>11</sup> The device consisted of an axially symmetric electrode configuration with a  $1.0 \pm 0.1$  cm hole in a molybdenum plate, and a center axial molybdenum wire  $0.5 \pm 0.1$  mm in diameter. The electrode configuration was connected directly to a  $2.4 \mu\text{F}$  capacitor and charged up to 4900 V as in Fig. 3. The electric charge was held due to the vacuum until the a laser initiated plasma expulsion off of a target near the electrode configuration allowed current to flow. The plasma jet forms due to the ablation of the molybdenum electrode and was measured when the current reversed direction from the capacitor discharge after  $\sim 4.4 \mu\text{s}$ . This is taken to be the  $t=0$  time of the jet formation.

The plasma from the coaxial plasma jet has been characterized with and without a magnetic field, but with the jet directed along the magnetic field.<sup>11</sup> Interferometry was used to measure the initial density of the jet. Velocities of the plasma jet were measured by following the morphology of the jet in the ICCD images, which is understood to be an approximate measurement. Velocities and densities of the plasma flow were also analyzed using electrical current flux tube analysis, matching the measured velocities and densities within an order of magnitude. Velocity, density and temperature are compared to similar values for cathode arc plasmas in literature, giving the estimate for temperature around 7 eV.<sup>12</sup>

We used both a magnetic dipole and an aluminum block as obstacles in the plasma wind path. The magnetic dipoles consisted of a permanent magnet cylinder with a radius of  $4.5 \pm 0.5$  mm and a length of  $9.0 \pm 0.5$  mm. The magnetic field strength as measured by a hall probe on the top of the pole was  $0.50 \pm 0.02$  T. The nonmagnetic obstacles were made out of aluminum and had the same dimensions. The  $4.5 \pm 0.5$  mm radius magnet was placed  $28 \pm 1$  mm away from the plasma source.

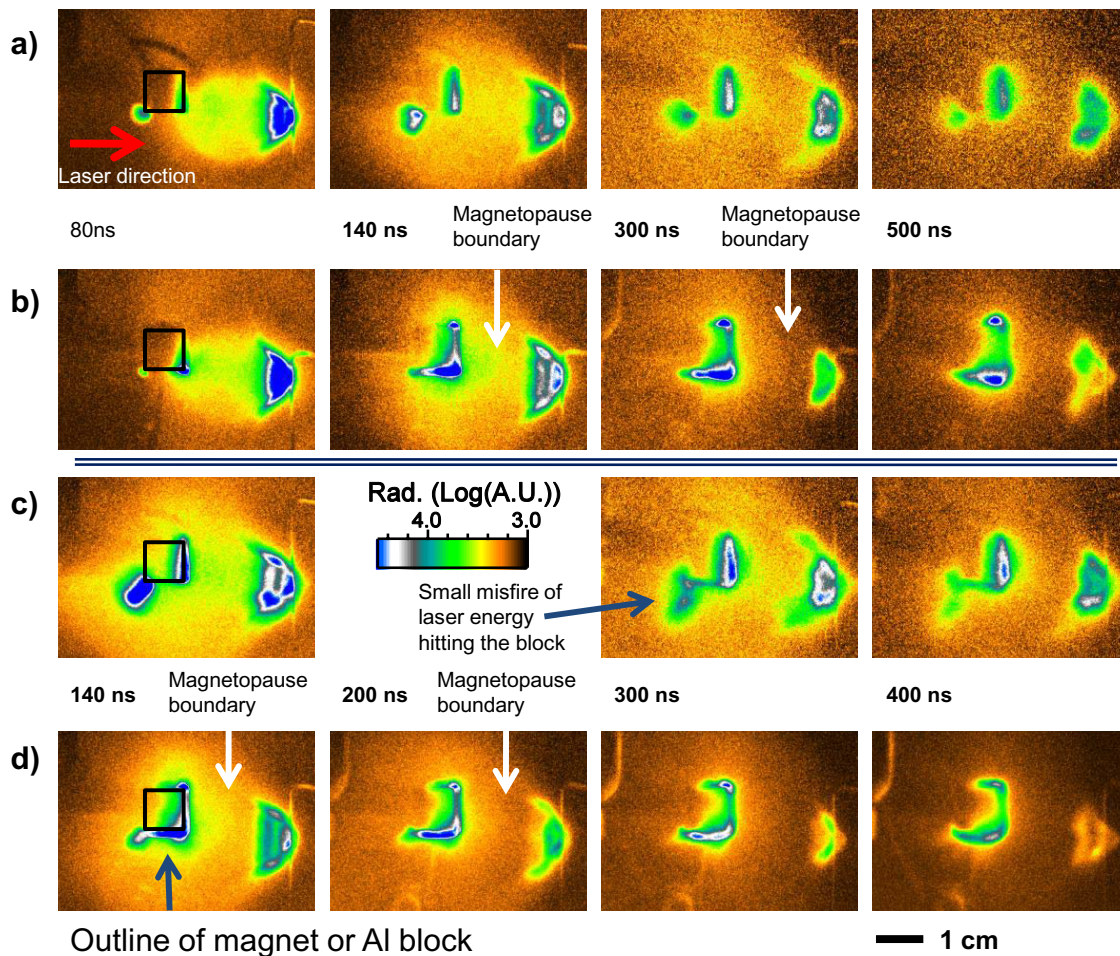


FIG. 4. (Color) 200 mJ laser pulse impinging on an Al target next to (a) a 4.5 mm radius Al block and (b) a 4.5 mm radius magnetic dipole. (c) and (d) have similar conditions as (a) and (b), respectively, with a 500 mJ laser pulse. The plasma wind flows from the right to the left of each frame (at the blue/green area) to the block in the frame middle. Plasma build up occurs on the face of the Al block in frames (a) and (c), whereas the plasma builds up on the polar cusp in the magnetic dipole case in frames (b) and (d). The magnetopause is marked on relevant images.

With the laser-produced plasma as the plasma wind the magnetic and nonmagnetic obstacles were placed in front of the laser target, as in Fig. 1. The obstacles were slightly off axis of the plasma wind to accommodate the laser beam path. The laser produced the blow-off plasma that flows back onto the obstacles along the same path that the laser traces out. When we used the coaxial electrode plasma jets as the plasma wind the obstacles were placed the same distance away from the plasma source as the laser-produced plasma experiment and the objects were placed directly on the axial path of the jet, as in Fig. 3.

#### IV. ANALOG OF SOLAR WIND AND MAGNETOSPHERIC DATA IN EXPERIMENT

We obtained data using an ICCD camera using the two plasma wind sources. As described in Sec. III we first used laser-produced plasma as a plasma wind source using 200 mJ, 500 mJ, and 2 J of energy in the laser pulses. Second, laser-triggered capacitor driven plasma jets were used as plasma wind sources using 3000 and 4900 V as parameters for the jets.

Measuring the magnetopause was the main goal of this project. The magnetopause manifest itself as a faint, but

measurable increase in plasma luminosity before the magnetic dipole in the laser-produced plasma experiment that is not observed in the aluminum block case, as in Fig. 4. As we will discuss in Sec. V the magnetopause is expected to be very close to the dipole before retreating in later parts of the expansion. Therefore we do not expect a highly evacuated region between the magnetopause and the dipole in this experiment, explaining the type of magnetopause we see in Fig. 4. The aluminum block had the plasma accumulation on the face of the block directly facing the plasma target interaction, as shown in Figs. 4(a) and 4(c). Plasma buildup along the poles also occurred with the dipole magnet, as shown in Figs. 4(b) and 4(d). This plasma buildup signified plasma buildup in the cusp region of a magnetosphere system. It can be seen from Fig. 4 that the laser hit the back of the magnet as it progressed toward the target. This should not be confused with a night side aurora. The build up of the plasma on the pole of the dipole is likely due to the flow of plasma frozen in magnetic field which is similar to the build up of the plasma on the cusp region of the Earth, which is distinct from the build up on plasma on the night side auroras. It is key to note that many planets do not have magnetic fields to protect them from the solar wind such as Venus. Thus the

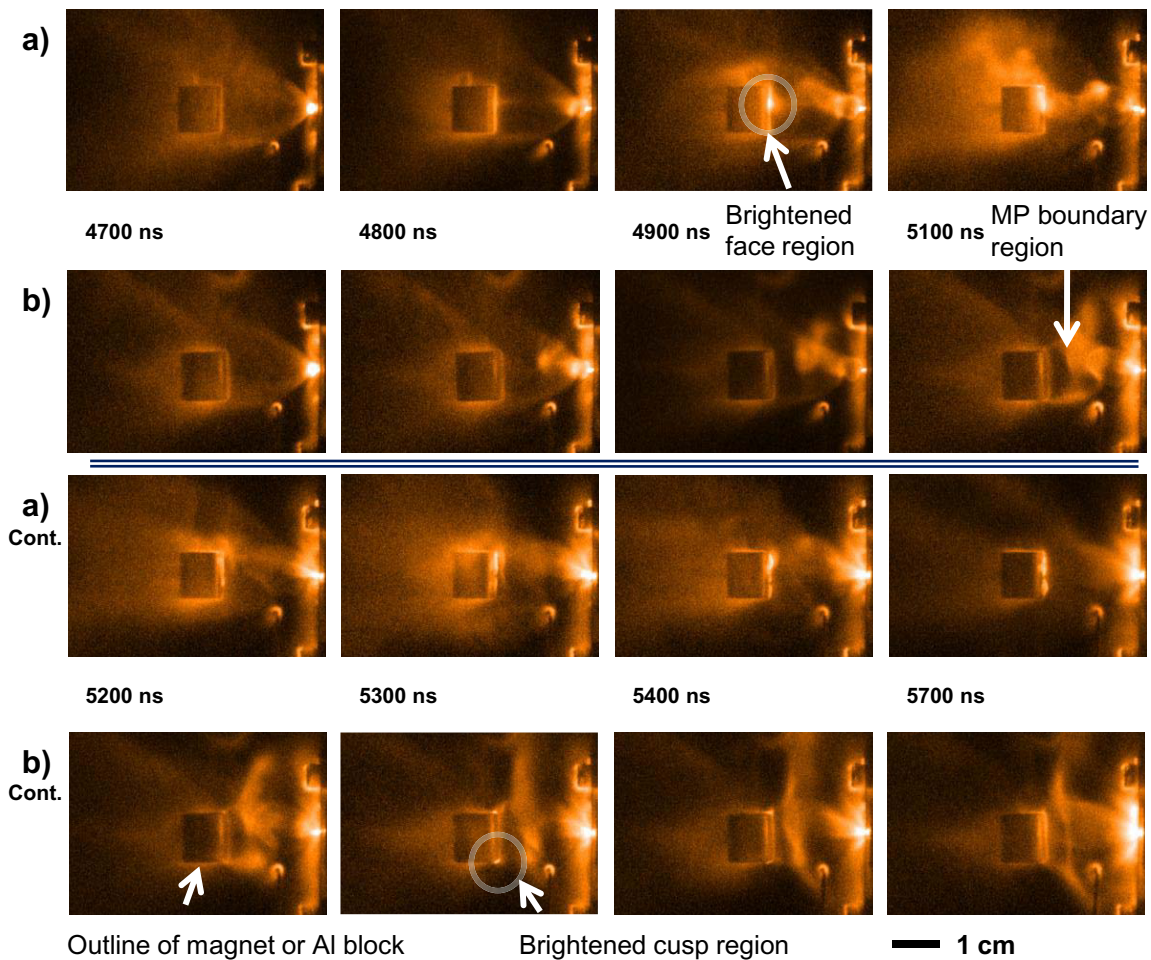


FIG. 5. (Color) Data for the magnetosphere experiment using a plasma jet from a capacitor driven coaxial electrodes charged to 4900 V for creating the plasma wind. The plasma wind comes from the right originating from the bright source on the right which is the coaxial electrode set up. Rows (a) and (a) cont. have an Al block and rows (b) and (b) cont. have a magnetic dipole of same dimensions for times 4700–5700 ns. The magnetopause can be seen in (b) from 4900 to 5700 ns. Plasma bombardment on the objects begins about 400 ns sooner with the aluminum block, than the magnetic field case due to the opposition of the plasma from the magnetic field pressure. The plasma bombardment is concentrated on the face of the aluminum block as in (a) and on the cusp regions of the magnetic dipole as in (b).

blocks with no magnetic fields represent an unmagnetized planetary ionospheric physics as on Venus.

A more distinct magnetopause and other plasma features are observed with the coaxial electrode plasma jet interacting with the magnetic dipole. Without an opposing magnetic field the plasma flows at a velocity of about  $3.9 \pm 0.2 \times 10^6$  cm/s.<sup>11</sup> One can see the plasma hit the Al block at a time consistent with this speed at the 4900 ns frame in Fig. 5 (recall that the jet begins at 4400 ns due to the electrical configuration of the jet) by brightening at the block face. Plasma illuminated the cusp region on the dipole at 5300 ns in Fig. 5 similarly to the plasma hitting the face in the non-magnetic example. Thus we see that the opposing magnetic field pressure in Eq. (4) slows down the plasma by about half the incident speed.

The capacitor driven jet material did not penetrate beyond the well defined magnetopause to the face of the dipole, as in Fig. 5(b). No such magnetopause was formed in the aluminum block case. The magnetopause radius reaches a fairly constant value of  $0.87 \pm 0.03$  cm in the 4900 V case over a period of about 1  $\mu$ s, as seen in Fig. 9(b). A plasma tail formed behind the magnet throughout the duration of the

jet which is a key characteristic of a solar wind-magnetosphere system (see Fig. 5).

We investigated the residue deposited on the magnet and blocks after a series of shots. The coaxial electrode jet experiments deposited much more material onto the block than did the laser-wire blow-off experiments. With the jet example the jet material plated half of the face of the poles of the magnet facing the jet, while the jet material plated only the surface of the side of the aluminum block facing the jet. This gives strong evidence that the jet material evolves according to magnetosphere dynamics.

## V. SIMULATIONS OF THE EXPERIMENT WITH HYADES

We used HYADES,<sup>13</sup> an one-dimensional Lagrangian hydrodynamic code developed at LLNL, to estimate parameters about the laboratory plasma wind. In our calculations we used 100 mesh points feathered at 5% over a length of 12.5  $\mu$ m with the feathered taper toward the laser source. We used the quotidian equation of state for aluminum with a density of 2.7 g/cm<sup>3</sup> and a bulk modulus of  $7 \times 10^{11}$  dyn/cm<sup>2</sup> and for copper with a density of 9.0 g/cm<sup>3</sup> and a bulk

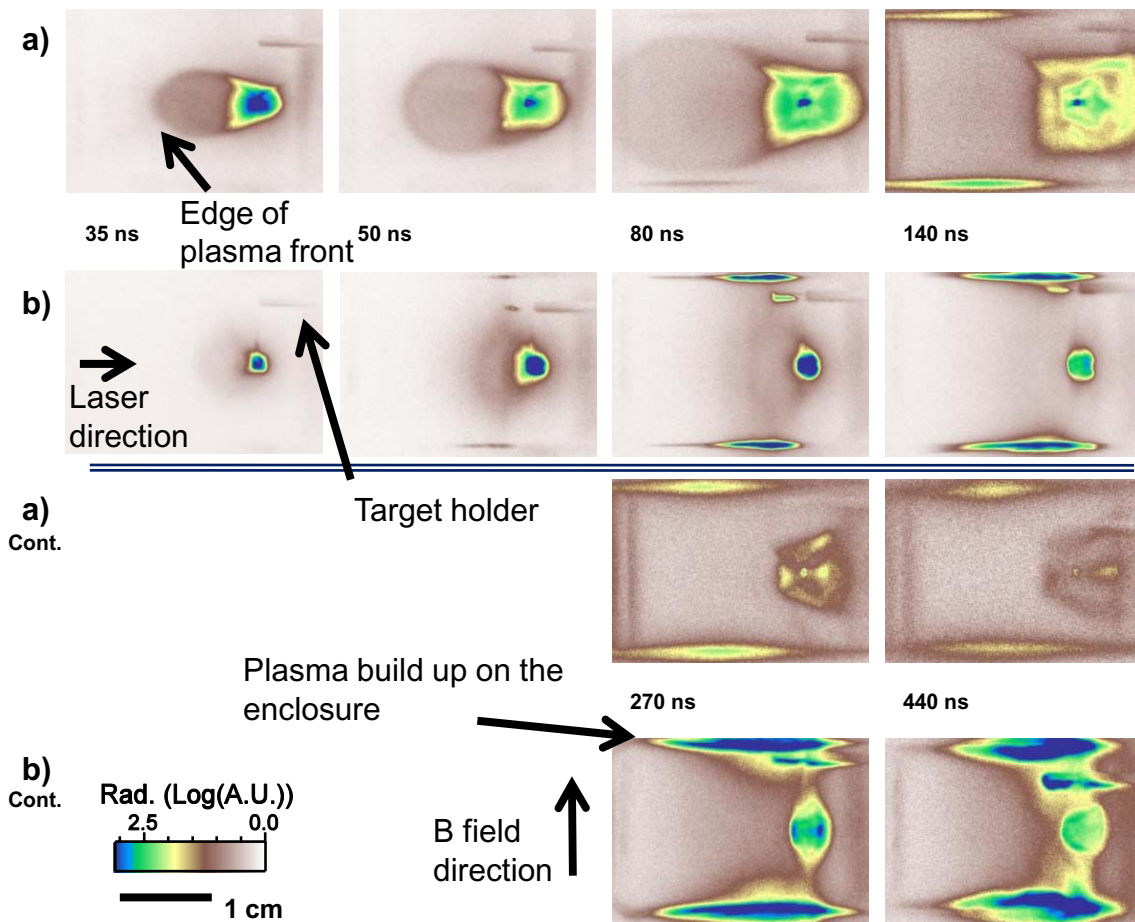


FIG. 6. (Color) ICCD image of laser-produced plasma progression where the input laser energy is  $\sim 200$  mJ and the target is  $\sim 25$   $\mu\text{m}$  thick Al wire. (a) is without  $B$  fields and (b) is with  $\sim 0.85$  T enclosed  $B$  fields. The laser comes from the right and the majority of the plasma flows to the left. The plasma front can be seen expanding in (a) at times 35–80 ns. The colder plasma dissipates in (a) in times 140–400 ns. Plasma stagnation can be seen from the magnetic pressure in (b) with significant build up on the poles of the magnet at times 80–440 ns.

modulus of  $1.4 \times 10^{12}$  dyn/cm<sup>2</sup>. We use both cylindrical and spherical geometries. For a typical calculation we use 0.2 J, 8.0 ns, 1064 nm laser source impinges on the 99th mesh point, with a Gaussian temporal profile and a 25 MW peak power. All of the HYADES simulations in this analysis did not use magnetic fields.

We performed several diagnostic tests using general laser-produced plasma to compare the HYADES code with laser-produced plasmas created in this experiment. Prior to conducting the magnetosphere experiment we ablated

25  $\mu\text{m}$  wire with the YOGA laser with and without a 0.85 T permanent magnetic field, as in Fig. 6. In addition to ICCD imaging we also used interferometry to measure the fringe shift at times less than 80 ns when the plasma density was high enough to detect. The laser-produced plasma expanded in an oblong form away from the target without the magnetic field, as in Fig. 6(a) with a well defined plasma front in the early parts of the expansion. In the 0.85 T magnetic field (in roughly the same order of magnitude as the dipole magnet, but uniform over a larger volume) the plasma expansion was

TABLE II. Comparison between the measured laser-produced plasma front distance as produced by a 1064 nm laser beam impinging on a 25  $\mu\text{m}$  diameter aluminum wire as compared to HYADES calculations in planar, cylindrical, and spherical coordinates.

| Time (ns) | Energy (mJ) | Measured length (cm) | Planar (cm) | Cylindrical (cm) | Spherical (cm) |
|-----------|-------------|----------------------|-------------|------------------|----------------|
| 35        | 20          | $0.64 \pm 0.10$      | 0.27        | 0.37             | 0.16           |
| 80        | 20          | $1.23 \pm 0.10$      | 0.68        | 0.88             | 0.32           |
| 35        | 200         | $1.18 \pm 0.10$      | 1.00        | 0.98             | 0.64           |
| 50        | 200         | $1.48 \pm 0.10$      | 1.48        | 1.47             | 0.87           |
| 80        | 200         | $2.36 \pm 0.10$      | 2.48        | 2.61             | 1.37           |
| 35        | 500         | $1.33 \pm 0.10$      | 1.51        | 1.33             | 1.02           |

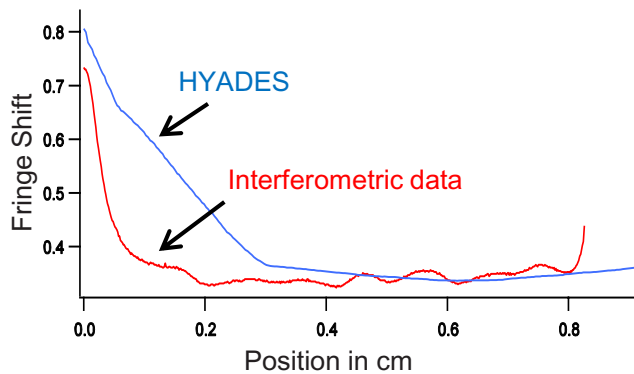


FIG. 7. (Color online) The fringe shift is compared to the line integral of the electron density from a cylindrical calculation from HYADES. The initial laser energy was 3.7 J on a 25  $\mu\text{m}$  copper wire and the expansion time was 50 ns.

significantly stagnated by the magnetic field pressure. Plasma build up on the poles of the magnet were similar to the magnetic dipole case. Thus we would expect comparable magnetic plasma behavior in the dipole case.

We calculated the plasma front of the laser-produced plasma expansion using HYADES and compared them to the experiment, as seen in Table II. Here HYADES simulated a laser ablated 25  $\mu\text{m}$  Al wire, slab, or sphere depending on the geometry and the outer plasma front that is visible in Fig. 6 was calculated. From this exercise we deduce that the cylindrical simulation best described the experiment, as the statistical match was best with the experiment. The geometry of the laser-produced plasma expansion is three dimensional

and not spherically symmetric, but does share similarities to the cylindrical and spherical expansions in HYADES.

HYADES was used to calculate the fringe shift, in cylindrical coordinates, according to

$$N = -2.38 \times 10^{-18} \text{ cm}^2 \int n_e dl, \quad (7)$$

with probing frequencies of  $\lambda = 532 \text{ nm}$  and where  $N$  is the multiple of  $2\pi$  that the fringe shifts in an interferogram,  $n_e$  is the electron density, and the integral is a line integral along the probe axis.<sup>14</sup> In Fig. 7 we measure the fringe shift of a 3.7 J laser pulse from the YOGA laser impinging on a 25  $\mu\text{m}$  copper wire. The fringe shift was obtained using a Wollaston prism interferometer with a probe frequency of  $\lambda = 532 \text{ nm}$ . The electron density from the HYADES calculation was line integrated to obtain the fringe shift and is shown together with the measured fringe shift in Fig. 7, showing less than 50% difference with the experiment. We have shown in these two experiments that HYADES can calculate meaningful results for various parameters and be compared with laser-produced plasma experiments.

We used the HYADES code to calculate laser-produced plasma parameters at 2 cm away from an Al target that had been ablated with a 200 mJ 1064  $\mu\text{m}$  laser source as a function of time. Linear extrapolations from the mesh output are reported in Fig. 8 with (a) the plasma pressure, (b) the plasma velocity, (c) the ion density, (d) the sound mach number, and (e) the electron density. From these parameters we calculated the standoff distance using Eq. (5) in three different ways in Fig. 9(a). We use both cylindrical and spherical

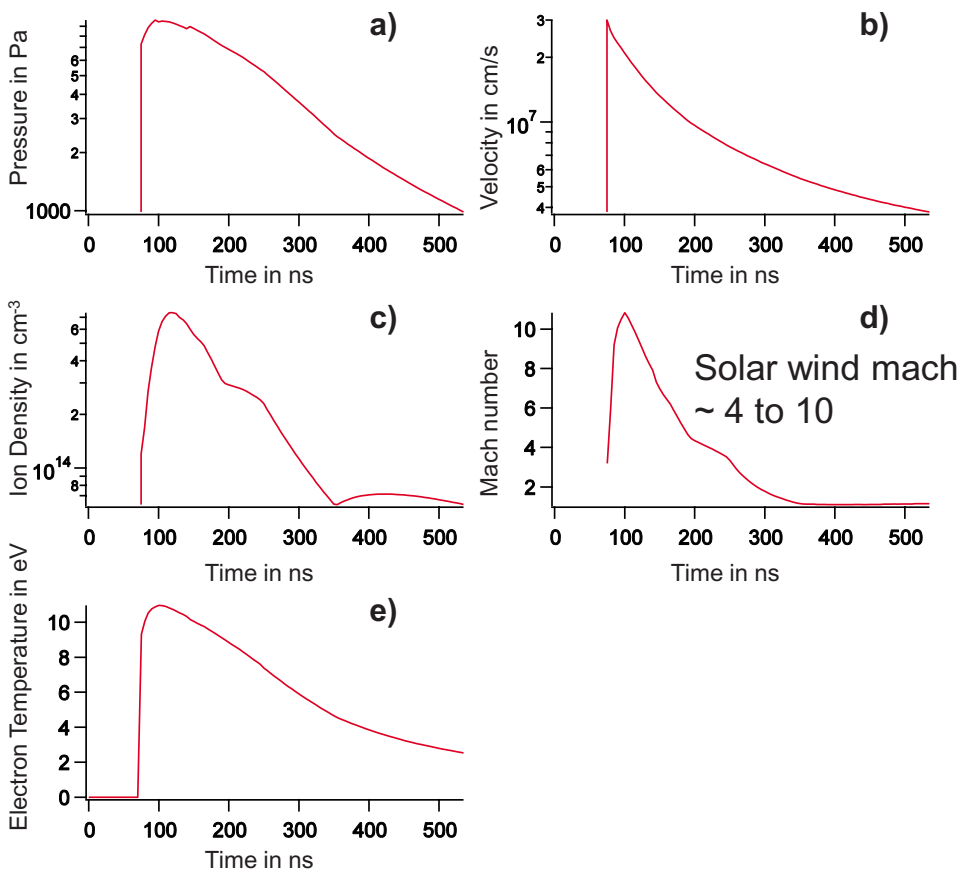


FIG. 8. (Color online) Simulation results for the five key plasma parameters for the plasma wind from a 200 mJ laser pulse impinging on an 25  $\mu\text{m}$  aluminum wire target at a distance 2.0 cm away from the ablated target. The simulation was in cylindrical geometry.

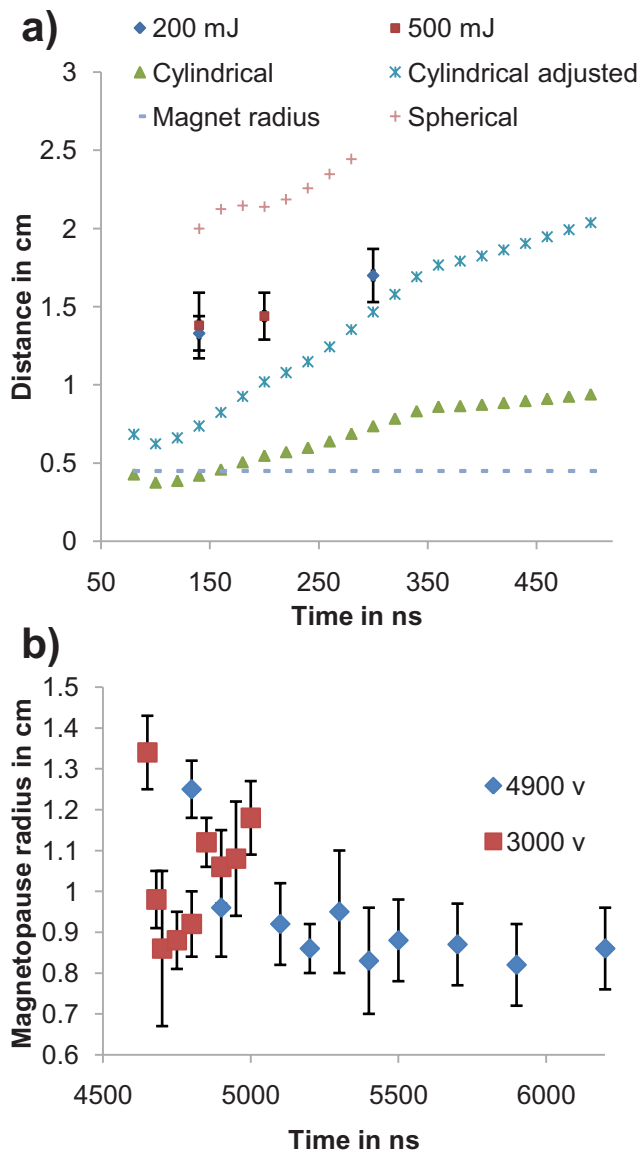


FIG. 9. (Color online) (a) Magnetosphere data from the laser-produced plasma experiments with HYADES calculations in both cylindrical and spherical cases, also with the cylindrical case adjusted for lateral expansion. (b) Magnetopause measurement from the coaxial plasma jet source with 4900 and 3000 V applied voltages.

calculations in Fig. 9(a) to simulate the magnetopause because there are inherent similarities of the cylindrical and spherical expansions to the actual laser-produced plasma expansion. Because of the similarities to both the spherical and cylindrical geometries we felt the need to include a solution between the two geometries. We impose dynamics in the axial direction of the cylindrical calculation by expanding the plasma at the 2 cm extrapolation point with the speed of the off-axial laser-produced plasma expansion of  $8.3 \pm 0.1 \times 10^4$  m/s observed in Fig. 6(a). The only parameter we then adjust is the density, and we keep the radially expanding velocity as is calculated by HYADES for simplicity. We then adjust the density calculated in the cylindrical HYADES calculation by multiplying the density with the ratio of the axially expanded plasma width as a function of time and the original  $400 \mu\text{m}$  laser focus spot size. We term this adjust-

ment as “cylindrical adjusted” in Fig. 9(a). We report that the adjusted cylindrical calculation was the closest to the measured magnetopause data with the spherical and cylindrical calculations being off by  $\sim 1$  cm in both directions. In comparison, the cylindrical calculations for the laser-produced plasma front are the best match to the measured laser-produced plasma front data in Table II.

The experimental magnetopause boundary is diffuse and difficult to measure as was expected owing to the finite value of the electron mean free path and the transient nature of the event. At 300 ns, the calculated magnetopause radii were  $0.74 \pm 0.02$ ,  $1.46 \pm 0.02$ , and  $2.54 \pm 0.02$  cm for the cylindrical, density adjusted cylindrical, and spherical calculations, respectively. The measured magnetopause radius was  $1.7 \pm 0.2$  cm. The adjusted cylindrical calculation matches the experiment best.

Data from HYADES can be used to calculate the force of the plasma wind on the magnets magnetosphere. If the magnetopause effective cross section was estimated to be  $4 \text{ cm}^2$  then the force on the magnetopause at 300 ns with a 200 mJ laser pulse would be

$$F_{\text{pw}} = A_{\text{mp}} P_{\text{pw}} \approx 1.2 \text{ N} \quad (8)$$

from the plasma wind. This would be a measurable force and we are interested in measuring this force in future experiments. Measuring this force would give important information about the size and effect of the magnetopause. As discussed in Sec. II this force caused the Chapman-Ferraro current to flow. The value of this current for the force calculated above will be 350 A using Eq. (6).

The magnetopause radius was measured from the ICCD data given in Fig. 5, and is reported for both 3000 and 4900 V jets in Fig. 9(b). The velocity of the upstream end of the plasma front in the magnetic dipole case, measured from the ICCD data, was  $1.7 \pm 0.2 \times 10^6$  cm/s. The densities of the jet were on the order of  $10^{15} - 10^{16} \text{ cm}^{-3}$  from various direct and indirect measurement in different conditions.<sup>11</sup> This gave a standoff distance of  $r_{\text{mp}} = 0.72 \pm 0.07$  cm for  $n = 10^{15} \text{ cm}^{-3}$  and  $r_{\text{mp}} = 0.49 \pm 0.05$  cm for  $n = 10^{16} \text{ cm}^{-3}$  from Eq. (5). The boundary of the standoff plasma measures to  $0.87 \pm 0.03$  cm over the measurements from 5100 to 6200 ns. This comparison showed that the two numbers are just beyond error for the  $n = 10^{15} \text{ cm}^{-3}$  case reflecting on the errors in estimating the density of the plasma.

The two situations scale hydrodynamically with three key dimensionless parameters:<sup>3-5</sup>  $a \approx 10^9$  (length scale ratio parameter),  $b \approx 10^{-15}$  (mass density scale ratio parameter), and  $c \approx 10^{-13}$  (pressure scale ratio parameter). The Euler number, or mach number, defined as  $E_u = u\sqrt{\rho}/P$  is another key descriptor in scaling.<sup>3</sup> The Euler number ranges from 5 to 10 for the solar wind-magnetosphere and 4 to 10 for the experiment. From the comparison we conclude that the solar wind-magnetosphere laboratory simulation offers a valuable scaling of laboratory-astrophysical data without the complications of gravity.

In laboratory comparisons with planetary magnetospheres one concern is that planetary magnetospheres are a collisionless phenomena and that the laboratory experiments are collisional. For much of the phenomena in the magneto-

sphere there would not be a good comparison of effects, but this is not the case for the magnetopause and the Chapman–Ferraro current investigated here. These effects are only dependent on the magnetization of the plasma and the effects of the flow of the plasma around the obstacle. Hence the degree of magnetization was the issue. The ions in these laser-produced plasmas and coaxial electrode plasma jets will not necessarily be magnetized but the electrons will be magnetized and will bind the ions to the magnetic fields through electrostatic forces. Thus, as seen with other magnetic effects in this series of experiments,<sup>11</sup> the experimental plasma wind will be affected by the magnetic dipole approximately, as described in Sec. II.

The magnetic Reynolds number,  $M_R$ , is important in determining how frozen the plasma is to the magnetic field lines and is important for scaling purposes. This quantity is given by  $M_R = \mu_0 L V \sigma$ , where  $L$  is the characteristic length,  $V$  is the characterization velocity, and  $\sigma$  is the electric conductivity of the plasma. The magnetic Reynolds number for the coaxial plasma jet parameters, with  $L = 0.01$  m,  $V = 4 \times 10^4$  m/s, and  $\sigma = 1.9 \times 10^4$  S/m, is  $M_R = 10$ . This meets Ryutov's condition for scaling of needing to be greater than one, but is not ideal and should be much greater than one to ensure reliable results.<sup>3</sup> The magnetic Reynolds number would be ideally much greater in the laboratory. For the laser-produced plasma experiment the magnetic Reynolds number, as based on the HYADES calculation at 300 ns with  $L = 0.01$  m,  $V = 7 \times 10^4$  m/s, and  $\sigma = 1.6 \times 10^4$  S/m, is  $M_R = 14$ , which is similar to the jet example. Hence the physics of the magnetopause between the two frames is on the edge of the similarity conditions. Also the Chapman–Ferraro current only needed a “jump” in the magnetic field to be produced, which will be provided by the laser-plasma wind compressing the magnetic field with the magnetized electrons.

The comparison between the magnetosphere frame and the experimental frame as calculated by HYADES is in Table I. There were no direct plasma parameter measurements in this experiment other than the ICCD camera imaging, but HYADES calculated reasonable values for density and front velocity in the laser-produced plasma that we substantiated with the laser-produced plasma experiments described in this section. With these HYADES results, the scaling between the two frames was similar with the Euler dimensionless parameter (also referred to as the Mach number) being similar between the two frames, being 5–10 for Earth's magnetosphere and 4–10 for the laboratory experiment.

The importance of laboratory simulations of magnetospheres can be emphasized by the relatively small spatial scale ratio of  $10^9$  of Earth's magnetopause as compared to other laboratory–astrophysical scaled experiments, and that gravity is not involved in the magnetopause formation. With this similarity scaling of key parameters and the geometrical similarity of the setup, further investigations into the dynamics of the laboratory magnetosphere plasma are warranted.

## VI. CONCLUSION AND FUTURE DIRECTIONS

We developed and performed repeatable laboratory experiments simulating supersonic plasma wind incident on a magnetic dipole target. The dynamics of wind–magnetosphere interaction were measured with both spatial and temporal resolution, opening up the possibility of direct investigation of relevant plasma dynamics of plasma wind on planetary and astrophysical objects. Found features were consistent with solar wind–magnetosphere interactions, including creation of a magnetopause in front of the magnetosphere, and brightening visible emissions at the magnetic poles with associated deposition on the polar caps of the targets. The observed diffuse magnetopause visible at the standoff distance is consistent with calculations of the standoff distance theory. Continued development of these techniques may provide valuable data for testing our current understanding of solar wind–magnetosphere and ionosphere interactions.

In comparing the magnetic dipole with the same sized aluminum block obstacle we see that the presence of the magnetic field increases the substantially effective area over which the incoming plasma wind is directed. This large area of diverted plasma flow increases the force on the obstacle approximately by the ratio of the area of the magnetopause to the area of the model planet. This is a substantial increase of the force on the model planet which we will measure directly in the proposed experiments through the forces on the connections used to suspend the model planets.

In future experiments the introduction of a tilt in the magnetic dipole similar to the Earth–Sun relationship will be made. Different tilts in the Earth–Sun system create different distributions of plasma around the magnetosphere, and these differences would be sought in the laboratory model. The incoming solar wind has an imbedded magnetic field that produces qualitatively different effects in the magnetosphere depending on whether the plasma wind's magnetic field is aligned or antialigned with the magnetosphere's magnetic field.<sup>15,16</sup> We propose to add magnetic fields in the laser-produced plasma by creating the plasma in a weak magnetic field. Differences would be expected in the plasma distribution around the dipole magnet with different directions of magnetic fields in the incoming plasma wind. This experiment would be similar to that in the Earth–Sun system, where strong changes in the interaction occur when the plasma wind magnetic field is opposite to that of the planetary magnetic field. Using  $B$ -probes in this experiment would give direct information about the magnetic field interactions with the plasma wind, magnetopause magnetic fields, and would potentially allow direct measurement of the Chapman–Ferraro current.

## ACKNOWLEDGMENTS

The research described in this publication was made possible in part by Grant No. RUP2-2683-NO-05 from the U.S. Civilian Research and Development Foundation for the

Independent States of the Former Soviet Union (CRDF) for the laboratory simulations of magnetospheric plasma shocks and particle acceleration, and by NSF Grant No. ATM-0638480 to the University of Texas at Austin.

- <sup>1</sup>W. Horton and C. Chiu, *Phys. Plasmas* **11**, 1645 (2004).
- <sup>2</sup>W. Horton, C. Chiu, T. Ditmire, P. Valanju, R. Presura, V. V. Ivanov, Y. Sentoku, V. I. Sotnikov, A. Esaulov, N. Le Galloudec, T. E. Cowan, and I. Doxas, *Adv. Space Res.* **39**, 358 (2007).
- <sup>3</sup>D. D. Ryutov, R. P. Drake, and B. A. Remington, *Astrophys. J., Suppl. Ser.* **127**, 465 (2000).
- <sup>4</sup>H. V. Cane and I. G. Richardson, *J. Geophys. Res., [Space Phys.]* **108**, 1156, DOI:10.1029/2002JA009817 (2003).
- <sup>5</sup>D. D. Ryutov and B. A. Remington, *Plasma Phys. Controlled Fusion* **44**, B407 (2002).
- <sup>6</sup>*Introduction to Space Physics*, edited by M. Kivelson and C. Russell (Cambridge University Press, Cambridge, 1995).
- <sup>7</sup>J. R. Spreiter and A. Y. Alksne, *Rev. Geophys.* **7**, 11, DOI: 10.1029/RG007i001p00011 (1969).
- <sup>8</sup>J. A. Ratcliffe, *An Introduction to the Ionosphere and Magnetosphere* (Cambridge University Press, Cambridge, 1972).
- <sup>9</sup>D. J. Williams, *Space Sci. Rev.* **34**, 223 (1983).
- <sup>10</sup>H. Alfvén, *Cosmic Plasma*, Astrophysics and Space Science Library, Vol. 82 (Kluwer, Boston, 1981).
- <sup>11</sup>P. C. Brady, Ph.D. thesis, University of Texas at Austin, 2008.
- <sup>12</sup>R. L. Boxman, P. J. Martin, and D. M. Sanders, *Handbook of Vacuum Arc Science and Technology Fundamentals and Applications* (Noyes, Park Ridge, 1995).
- <sup>13</sup>J. T. Larsen and S. M. Lane, *J. Quant. Spectrosc. Radiat. Transf.* **51**, 179 (1994).
- <sup>14</sup>R. H. Lovberg and H. R. Griem, *Methods of Experimental Physics*, Vol. 9 Plasma Physics (Academic, New York, 1971), Pt. B.
- <sup>15</sup>T. W. Hill, in *Quantitative Modeling of Magnetospheric Processes*, Geophysical Monograph Series (American Geophysical Union, Washington, D.C., 1979), pp. 297–315.
- <sup>16</sup>J. W. Dungey, *Phys. Rev. Lett.* **6**, 47 (1961).